creative commons
COMMONS DEED

저작자표시-비영리-변경금지 2.0 대한민국

이용자는 아래의 조건을 따르는 경우에 한하여 자유롭게

- 이 저작물을 복제, 배포, 전송, 전시, 공연 및 방송할 수 있습니다.

다음과 같은 조건을 따라야 합니다:

저작자표시. 귀하는 원저작자를 표시하여야 합니다.

비영리. 귀하는 이 저작물을 영리 목적으로 이용할 수 없습니다.

변경금지. 귀하는 이 저작물을 개작, 변형 또는 가공할 수 없습니다.

- 귀하는, 이 저작물의 재이용이나 배포의 경우, 이 저작물에 적용된 이용허락조건을 명확하게 나타내어야 합니다.
- 저작권자로부터 별도의 허가를 받으면 이러한 조건들은 적용되지 않습니다.

저작권법에 따른 이용자의 권리는 위의 내용에 의하여 영향을 받지 않습니다.

이것은 이용허락규약(Legal Code)을 이해하기 쉽게 요약한 것입니다.

Disclaimer

dCollection

RESEARCH TITLE

이학석사 학위논문

Atomistic origins of mechanical amorphization of SiO_2 using solid-state ^{29}Si NMR and local electronic structures for SiO_2 high pressure phases using *ab initio* calculation

기계적 비정질화된 실리카의 실리콘 원자 주변 고상 핵자기 공명 분광분석과 고압 동질이상 결정질 실리카의 전자구조 양자계산 연구

2017 년 1 월

서울대학교 대학원

자연과학대학 지구환경과학부

김 훈

Atomistic origins of mechanical amorphization of SiO_2 using solid-state ^{29}Si NMR and local electronic structures for SiO_2 high pressure phases using *ab initio* calculation

기계적 비정질화된 실리카의 실리콘 원자 주변 고상 핵자기 공명 분광분석과 고압 동질이상 결정질 실리카의 전자구조 양자계산 연구

지도교수: 이성근

이 논문을 이학석사 학위논문으로 제출함

2017 년 1 월

서울대학교 대학원
자연과학대학 지구환경과학부

김 훈

김훈의 이학석사 학위논문을 인준함.

2017 년 1 월

위 원 장 이 준 기 (인)

부위원장 이 성 근 (인)

위 원 김 영 희 (인)

Contents

ABSTRACT

Silica (SiO_2), the most abundant material on the earth, is a major component of the crust and mantle. Therefore the structure of silica affects the dynamic process of crust or the structural properties of the earth interior. The structure of silica changes not only by pressure-temperature change but also mechanical energy like friction without melting. To understand the properties of interior of rocky planets and the geological process, the detailed understanding of the structure of silica with various conditions is needed. In this study, we performed two major subject related to structure of silica.

The first study is about atomistic origin of the mechanical amorphization of silica with an experimental methodology. There have been reported the reduction of fault strength during fault slip, and one of the causes is reported as the formation of the amorphous silica and the silica gel layer on the fault plane. The formation of amorphous silica is due to the frictional energy between the fault surfaces, and the formation of silica gel layer is due to reaction with the water present in the layer or air. In previous, studies on frictional experiments using quartzite rocks, reported the formation of silica and silica gel and also the decrease of friction coefficient, and the observation of the silica gel layer in natural faults has been reported. However, due to the complex structure of amorphous silica and the analytical method limitations, the atomic structure of the amorphized silica and the detailed origin of the mechanical amorphization process have not been clearly identified. In this study, silica was amorphized with mechanical energy by ball mill method, and the resulting amorphous structure was analyzed by high resolution nuclear magnetic resonance (NMR) spectroscopy. The morphology of the amorphized silica and the phases formed by other elements were analyzed using XRD, HR-TEM, and EDS-mapping method.

Solid-state nuclear magnetic resonance spectroscopy (NMR) is suitable for the analysis of complex amorphous structures because it yields atomic environments in short range order around specific atoms and provides quantitative information on atomic unit bonding. The ^{29}Si MAS NMR spectra of amorphous silica milled at different rates present that the spectra of samples milled above 600 rpm show a broad amorphous peak over -80 to -120 ppm. These amorphous peaks indicate the presence of Q^2 and Q^3 structures in the mechanically amorphized silica. The results indicate that the mechanical amorphization of silica occurs only above a certain energy level, and that the amorphization process results in a change in the short range atomic structure and imply the presence of reaction with other elements. This results help to understand the atomic structure of the mechanically amorphized silica and the mechanical amorphization process that occurs without melting in the fault plane.

The second study is an electronic structure and detailed origin of spectral feature of O *K*-edge XRS for crystalline silica using computational computation. Crystalline silica undergoes various phase transition according to pressure-temperature change. Therefore, many studies on the structure of high-pressure phase silica have been reported to understand the internal structure of rocky planets in high temperature and high pressure environment. The most powerful method of in situ high-pressure study for electronic structure is O *K*-edge x-ray Raman spectroscopy (XRS) using diamond anvil cell and as experimental limitation above ~70 GPa, the computational methods is used to understand the XRS spectrum. However, the detailed relation between spectral feature of O *K*-edge XRS and structure is still in debate.

In this study, we calculated electronic structures and O *K*-edge XRS spectra for various crystalline silica using *ab initio* calculation, and proved the origin of O *K*-edge XRS spectrum. Previous studies have suggested that the origin of the O *K*-edge XRS spectrum is

attributed to the number of Si atoms or the number of O atoms. However, in this study, we have found that the O *K*-edge XRS spectra of hp-cristobalite with 4-coordination Si, of penta-SiO_2 with 5-coordination Si and of stishovite with 6-coordination Si are similar, and O site resolved *K*-edge XRS spectra the penta-SiO_2 revealed that the coordination of atoms does not directly affect the O *K*-edge XRS spectral feature. These results not only provide an understanding of the electronic structure of high-pressure phase silica, but also provide clear criteria for O *K*-edge XRS spectral analysis.

Keywords: silica, nuclear magnetic resonance (NMR), ball mill, mechanical amorphization, high-pressure phase, *ab initio* calculation, O *K*-edge XRS.

LIST OF FIGURE

Figure A1. Ground sate PDOS for each crystallographically distinct atom orbital of α-quartz (a), β-quartz (b), α-cristobalite (c), coesite (d), hp-cristobalite (e), penta-SiO_2 (f), stishovite (g), $CaCl_2$-type (h) and pyrite-type (i).

Figure A2. Excited sate of crystallographically inequivalent O atom PDOS for each SiO_2 polymorphs. The total PDOS for calculate SiO_2 polymorphs (a) and the site resolved PDOS for coesite (b) and penta-SiO_2 (c).

LIST OF TABLE

Table 1. Si atom coordinates, Space groups, lattice parameter and structural variables of SiO_2 polymorph

[a]High-resolution synchrotron-radiation powder data for crystalline quartz (Will et al., 1988)

[b]X-ray diffraction for crystalline quartz at temperature ranging from 298 K to 1126 K (Kihara, 1990)

[c]Neutron time-of-flight and X-ray Guinier diffractometry (Schmahl et al., 1992)

[d]X-ray diffraction for coesite (Levien and Prewitt, 1981)

[e]Ab initio calculations (Huang et al., 2006)

[f]Ab initio calculations (Badro et al., 1997)

[g]X-ray diffraction (Yamanaka et al., 2002)

[h]X-ray diffraction under pressure ~63 GPa (Andrault et al., 1998)

[I]X-ray diffraction under pressure ~271 GPa (Kuwayama et al., 2005)

1. INTRODUCTION

Silica (SiO_2) is one of the most abundant natural materials in the Earth's crust and mantle, and has long been studied because of their importance in geology as well as material science. Even though the chemical composition of silica is very simple, the structures vary considerably, upon which their properties depend, with changing P-T conditions and dynamic process of the Earth. For instance, the dynamic movement of crust, accompanied by enormous friction with large kinetic energy, also cause the structural changes of silica (crystalline → amorphous) (Nakamura et al., 2012), which commonly occur with hydration in natural fault zones. The crystalline structure of SiO_2 change with increasing pressure (*a*-quartz → coesite → stishovite → $CaCl_2$-type → *a*-PbO_2-type → pyrite-type) (Kuwayama et al., 2011; Wu et al., 2011), and these structural changes accompanied by changes in the Si coordination cause changes in properties such as elastic constants. Despite these geological significance and importance, many questions related to the structure of SiO_2 have not yet been solved. In this study, we range over the two topics of detailed SiO_2 structure using experiment and calculation methods.

The first section presents the atomistic origin of mechanical amorphization mechanism of SiO_2. The frictional weakening of fault during slip has been reported in many studies. This frictional strength reducing mechanism is call the slip weakening and various processes have been suggested as causes (gauge lubrication, thermal decarbonation, frictional melting and silica gel formation). Since most of the rocks are composed of SiO_2, there are many studies on the silica amorphization and silica gel formation due to friction (Di Toro et al., 2004; Power and Tullis, 1989). However, due to the complexity of the amorphous structure and the limitation of spectroscopy, the understanding of detailed

knowledge about mechanical amorphization process of SiO_2 is still unclear. Therefore we report the detailed analysis of mechanically amorphized structure of SiO_2, with different mechanical energy using ball mill method, using solid-state nuclear magnetic resonance (NMR), which provides the short-range structure of specific atom making possible to understand the amorphous structure.

The second section presents the electronic structure of crystalline SiO_2 polymorphs and O *K*-edge x-ray Raman scattering (XRS) spectrum of each crystal phase. Since SiO_2 is the most fundamental component in both Earth and super-earths, which consist of rocky materials, understanding of the structural change of SiO_2 is essential to understand the internal structure of those planets. The electronic structure of SiO_2 high-pressure phase can be explored by O *K*-edge XRS using high-pressure diamond anvil cell (DAC) experiment or *ab initio* calculation (Fukui et al., 2009). However the clear link between the spectral feature of O *K*-edge XRS and crystalline SiO_2 structure has not been suggested. Therefore we report the O *K*-edge XRS spectrum for SiO_2 polymorphs, which possess Si coordination of five and six, and the precise origin of O *K*-edge XRS spectrum.

2. THEORETICAL BACGROUNDS

2.1 NMR techniques

Nuclear magnetic resonance (NMR) is an element-specific probe, which provides molecular structure of specific element from interaction of the nucleus spin and magnetic fields. The fundamental principle of NMR is similar to that of the magnetic resonance imaging (MRI), the differences between two methods are the strength of magnetic field of the machine and the size of samples. The samples used for MRI are usually humans and animal, while for NMR are various experimental liquid or solid compound which size range millimeters to a few centimeters. The magnetic field of clinical MRI almost are 1.5 T (Tesla) and 3.0 T, while that of NMR ranges from 4.7 to 23.5 T.

The NMR have been used to analysis crystal structure of organic compounds in liquid phase, However the nuclear spin in solid-state does not tumble in random direction as they do in liquid-state, and which cause the quadrupolar coupling effect broadening line-widths of NMR spectrum. To overcome this quantum mechanical perturbation, special techniques like magic angle spinning (De La Pierre et al.), dynamic angle spinning (DAS) and multiple quantum transition MAS (MQMAS) developed and allowed studies in solid-state NMR (SSNMR) increase. Since those techniques developed, NMR spectroscopy has become one of the important methods to study geology and material science.

Because NMR can detect nuclear magnetism which is very weak but sensitive to electronic structural change of material, its utility for characterizing structure of amorphous material and glasses is superior to any other spectroscopic methods. Furthermore, because NMR detects specific nuclear magnetism, it can provide the relative amount of specific elements (i.e. relative amount of aluminum in aluminosilicate) and distinguish the relative

amount of aluminum which exist in different coordination. In addition, using H1 MAS NMR, we can distinguish acidic site.

2.2 Ball mill method

There are various kinds of milling methods depending on capacity, additional arrangements for cooling and heating, and all have been used to make various alloy powders or ceramic powders. In this paper, however, only the method we used in the experiment (planetary ball mill) is explained. The term 'planetary ball mill' originated from its planet-like movements of its vials (movement of orbit and rotation of planets). The centrifugal forces produced by both the vial and the support disk act on the sample inside of the vial, because the rotation axis of vial is arranged on the end of the bottom disc and the direction of rotation of the vials is opposite to that of the lower disc, and rotate alternately. The grinding balls inside the rotating vial moves along with the vial wall and causing friction to the materials (the friction effect), or falling off the vial wall and colliding with the materials on the opposing inside wall (the impact effect) (Suryanarayana, 2001).Thus, the faster the spinning speed, the higher mechanical energy can be applied to the sample, and the higher mechanical energy applied to the sample produces amorphous alloy powder of metals with a high activation energy barrier or amorphous ceramic powder in metastable states. This mechanism applies high mechanical energy to the materials and produces amorphous alloy powder of metals with a high activation energy barrier or amorphous ceramic powder in metastable state. There are eight types of substances used to make vials and ball (agate, silicon nitride, sintered corundum, zirconia, chrome steel, Cr ± Ni steel, tungsten carbide, and plastic polyamide) (Suryanarayana, 2001), and all of which are resistant to friction and impact and are not easily react with the sample materials.

2.3 *Ab initio* calculations

The word '*ab initio*' is a Latin term meaning the start from the beginning, and the *Ab initio* calculation, which also used called as first-principle methods, solves equations with only fundamental law of nature and no empirical relations. Most of the quantum chemical calculations is based on *ab initio* techniques, because the detailed correlations of quantum particles are only explicable in terms of math. Understanding of the electromagnetic interactions within the structure is essential to understand the electronic structure of matter and the *ab initio* calculation derives the electronic structure of interest object by solving the wave equation, which explains the electromagnetic interactions among electrons and protons.

However, the present computer technology still has many limits in solving the complex wave equation, which have to consider all the interactions between electrons. Therefore ab initio calculation use modeling methodology called density function theory (DFT), one of the most prevalent methods to process *ab initio* calculations, considering many-electron system as electron density and increase the computational efficiency. Specifically using DFT the many-body problem of interaction electrons becomes simple by presume electrons as electron density with Kohn-Sham equations, and which make computing resources for calculations much less(Kohn and Sham, 1965; Schwarz, 2003; Tse, 2002). Then the calculation became more efficient by approximating both exchange energy and correlation energy with an exchange-correlation potential.

In the electronic structure calculation using the DFT theory, the approximation method of exchange-correlation energy determines the accuracy of the *ab initio* calculation. The local density approximation (LDA) is the most simple approximation method of electronic structure, which approximates the exchange-correlation function only using electron density ($\rho_{\uparrow\downarrow}$) making calculation efficient, and show good calculation results for

materials with small number of electrons and small changes in electron density. Since the generalized gradient approximation (GGA) method, on the other hand, express the exchange-correlation function as a function of the electron density ($\rho_{\uparrow\downarrow}$) and the derivative of electron density ($\bigtriangledown\rho_{\uparrow\downarrow}$), present more accurate electronic structure for low-*z* elements materials, made of atoms with a small number of electrons. In this study, we calculated using GGA-PBESOL method, which is one of the most optimized GGA methods for calculating the electronic structure of solid materials, proposed by Perdew, Berke and Ernzerhof (Perdew et al., 2008).

The two methods for calculate the electron orbital, pseudo-potential (PP) method and the FP-LAPW method, are widely used in the first principle calculation studies. The PP method increases the calculation efficiency by approximating interaction between core and core electron as the pseudo potential. For this reason, PP method is not suitable for calculation of core level spectroscopy, which stems from the excitation of core electrons and has strong correlation with the electronic structure near the atomic nucleus, such as nuclear magnetic resonance (NMR) spectroscopy or x-ray Raman scattering (XRS). On the other hand, the FP-LAPW method expresses all electrons, including core electrons, using the LAPW basis function and not approximates the core electrons as a quasi-potential, and which makes it suitable for calculation of the core level spectroscopic spectra like NMR or XRS. In this study, therefore, we used the WIEN2k program which use FP-LAPW method to calculate O *K*-edge XRS spectra for SiO_2 polymorphs (Blaha et al., 2001; Schwarz, 2003).

3. ATOMISTIC ORIGINS OF MECHANICAL AMORPHIZATION BY BALL MILL EXPERIMENTS: INSIGHTS FROM Si-29 NUCLEAR MAGNETIC RESONANCE

3.1. Introduction

SiO_2 is the most basic Earth-material composed of Si and O, which are the most abundant elements in the crust, and directly related with the dynamic process of the crust. The frictional strength between the fault planes, the change of which are caused during the fault slip, has been an important subject in fault mechanism studies. The slip weakening is a fault mechanism of fault strength weakening during accelerated slip in the fault plane. These dynamic reduction of fault strength can cause serious earthquake rupture and has been studied by many theory and laboratory experiments. The formation of gauge (fine-gran rock powder formed by friction on fault plane) have been reported, by rotary shear experiment on granite disk, as one of the causes of slip weakening by acting as lubrication on fault plane (Reches and Lockner, 2010). The thermal decomposition of carbonate has been reported as a process for slip weakening, as this process produce nanometer sized fine particle (Han et al., 2007). The frictional melting with the formation of pseudo-tachylytes also suggested as the reason of dynamic weakening of faults (Kanamori et al., 1998).

In addition, since quartz is one of the most abundant minerals that constituting the Earth's crust, there have been many studies on slip weakening with quartz rocks. The extraordinary progressive decrease of frictional strength of quartz rock with slip velocity above 1 mms^{-1} have been reported, and the formation of a thin layer of silica gel is suggested as the reason of reduction of frictional resistance, and the formation of silica gel appears to be due to the formation of amorphous SiO_2 on the frictional plane. (Di Toro et al., 2004; Di Toro et al., 2011). The formation of amorphous silica and decrease of frictional resistance on quart rock, even under a small load (1N), have been reported using FT-IR and Raman

mapping, and they also suggested under high pressure condition the amorphization could occur even in a smaller slip distance, which could trigger the accumulation of glassy gouge during aseismic fault creep or slow slip events (Nakamura et al., 2012). Furthermore, the observation of a natural silica gel layer (composed of ~100 nm to 1 nm grains of quartz, hydrous crystalline silica and amorphous silica with 10-100 nm inclusion of Fe oxide and ellipsoidal silica colloids.) on fault surface at Corona Height fault has been reported, confirming that the reported silica gel formation in shear experiments really do occur on natural fault plane (Kirkpatrick et al., 2013).

There are many friction experiments and the observation in the natural fault of quartz rock have reported the formation of silica gel and amorphization of SiO_2, with its importance on the slip weakening mechanism. However, few have been studied on atomistic analysis of origins of mechanical amorphization of silica, because many spectroscopic method doesn't provide detailed short-range structure of amorphous materials. So the understanding of the detailed process by which crystalline SiO_2 mechanically becomes amorphous SiO_2 remains unclear.

Here we report the detailed analysis on mechanical amorphization process of SiO_2 using high-resolution solid-state Si-29 MAS NMR, which can yields the information of short-range structure near Si atoms. Using ball mill method, powerful method for synthesis amorphous alloys and ceramic amorphous phases in powder form, amorphous silica was produced without any melting process. Amorphous SiO_2 was formed without any melting process by using the ball mill method at four speeds (200, 400 600, and 800 rpm) for the analysis of the relation between different mechanical energy upon SiO_2 and amorphization mechanism.

3.2. Experiments

3.2.1 Sample Preparation and Analysis

The crystalline SiO_2 powder (*a*-quartz, from sigma-aldrich) was prepared to perform the mechanical amorphization experiments using planetary ball mill method. The crystalline SiO_2 powder and ball milled SiO_2 powders (with different four milling speed) were analyzed using Si-29 MAS NMR, x-ray diffraction and field emission scanning electron microscope (FE-SEM) to confirm its morphology and figure out its detailed structure. Also the chemical characteristics and detailed morphology of the ball milled SiO_2 powder was investigated with additional different techniques, high resolution transmission electron microscope (HR-TEM) and energy dispersive x-ray spectroscopy mapping.

3.2.2 Planetary Ball Mill

The samples were ball milled in a planetary ball mill machine (model PULVERISETTE 7 manufactured by FRITSCH GimbH in Germany) at Electrochemical Energy Conversion & Storage Laboratory. The vials that contain the sample and grinding balls are all made of ZrO_2. Prior to the milling experiments, the fumed silica (~14 nm) was milled at 800 rpm for 10 h to completely clean the inside of the vials to prevent any chemical reaction between the sample and impurities during the ball milling process. In order to confirm the amorphization mechanism of SiO_2 with increasing mechanical energy, experiments were performed for four different milling rotational speed (200, 400, 600 and 800 revolution per minute, rpm). All experiments were performed for 5 hr net milling time, and to prevent overheating of the ball mill machine, 30 min was given as rest time in every 30 min milling time, so each milling experiment was conducted for 10 hr in total. The sample amount is 600 mg and ball is 9.2 g, so ball to powder ratio (BPR) is about 15. We also

performed experiment with the inside of the vial filled with Ar air, in order to compare the experiment with prevented SiO_2 from reacting with H_2O component in the air during the ball milling process. The Ar environmental milling experiment was prepared by drying the crystalline SiO_2 at 120 °C for 12 h and then sealing the vial in the Ar environment, and ball milled with 800 rpm for 10 h. All ball milled SiO_2 samples are fine white powder composed of particles smaller than few tens of nanometers.

3.2.3 NMR Spectroscopy

Si-29 MAS NMR spectra for ball-milled SiO_2 were collected on a Varian400 MHz solid-state spectrometer (9.4 T) at a Larmor frequency of 79.4705 MHz using Doty MAS prove with 4 mm zirconia rotor (spinning speed of 12 kHz). All spectra were referenced to tetrametylsilane (TMS). A single-pulse sequence with an approximately 30-degree pulse (1.6 μs) were used, and different delay time were used depending on its purpose, 10s to check amorphous structure and 4200s to check crystalline structure.

3.2.4 X-ray Diffraction

X-ray Diffraction (XRD) experiments were performed with Rigaku Minflex 300/600 using Cu *K*α radiation (wavelength λ = 1.6 Å). Data were collected at room temperature in the angular range 5-90° in 2θ, and step degree 0.02° with continuous mode. The voltage and current are 40 kV and 15 mA, respectively. The step speed for ball-milled SiO_2 was 1.0°.

3.3. Results and Discussion

3.3.1. TEM EDS

Figure 1 shows the images of 600 rpm ball milled SiO_2 particles and the EDS mappings for Si, O and Zr elements. The particle size of ball milled SiO_2 is not homogeneous and most of the particles are smaller than 1 nm. While the specific element EDS mapping images show that the most part of the sample consist of Si and O element, indicating amorphous and crystalline SiO_2. The Zr elements EDS mapping represents the Zr peaks are scattered on the ball milled SiO_2 particles and ZrO_2 fragments. The bright part in dark field TEM image is the part composed of Zr elements with relatively many electrons. These images suggest that during the milling of crystalline SiO_2 with ZrO_2 balls, with milling speed of 600 rpm, accompany breakages of ZrO_2 balls

3.3.2. X-ray Diffraction Patterns

Figure 2A presents the XRD pattern for crystalline SiO_2 (*a*-quartz) and ball milled SiO_2 with different condition and same milling speed of 800 rpm. The Ar environment ball milling was performed to investigate any H_2O effects on mechanical amorphization during ball milling. Although there are significant increase of amorphous structure on SiO_2 after severe milling, XRD pattern still indicate the existence of crystalline SiO_2, without any evidence for H_2O effects. However, XRD patterns for the ball milled SiO_2 with milling speed of 800 rpm show the existence of ZrO_2 component, which must came from the grinding medium, ZrO_2 balls. Figure 2B shows the XRD pattern for crystalline SiO_2 and ball milled SiO_2 with different milling speed, 200, 400, 600 and 800 rpm. The crystalline SiO_2, prior to ball-milling, shows sharp diffraction peaks of α-quartz. These results also represent the increase of amorphous phases with increase of milling speed and especially rapid increase of

amorphization above 400 rpm. Also, the ZrO_2 fragment increase with increasing milling speed because increase mechanical energy caused more breakages on ZrO_2 balls.

3.3.3. Si-29 MAS NMR

Figure 4 shows the ^{29}Si MAS NMR spectra of ball milled SiO_2 with delay time of 10 sec. While all other ^{29}Si MAS NMR spectra of ball milled SiO_2 show clear amorphous phases with broad peak ranging from – 120 ppm to -80 ppm, the ^{29}Si MAS NMR spectrum of ball milled SiO_2 with 200 rpm shows single sharp peak at -107.5 ppm, confirming there were little mechanical amorphization with 200 rpm and it still mostly consist of crystalline *a*-quartz. Considering that the Q^2 and Q^3 species positions in ^{29}Si MAS NMR spectrum are -91.4 and -101.6 ppm respectively(Kim and Lee, 2013), the amorphous structure of ball milled SiO_2 consist of Q^2, $Q^3$and Q^4 species, which suggest mechanical energy caused increase of short range disorder in SiO_2

Figure 5 shows the ^{29}Si MAS NMR spectra for ball milled SiO_2 with 200 rpm and 800 rpm and ball milled SiO_2 with 800 rpm in Ar environment, with delay time of 4200 sec to investigate the crystalline structure in amorphous SiO_2. While the ^{29}Si MAS NMR spectra of both 800 rpm ball milled SiO_2 show distinct broad spectrum of amorphous SiO_2, crystalline peak at -107.5 ppm still exist, indicating the complicated structure of amorphous and crystalline phases. This Ar-environment milling experiment was designed to confirm any H_2O in atmosphere effects on mechanical amorphization mechanism. As there are any spectral difference between ball milled SiO_2 and Ar-environment ball milled SiO_2, we can confirm there were little influence of H_2O in atmosphere.

Figure 6 shows the ^{29}Si MAS NMR spectra for ball milled SiO_2 with different milling speed. While all spectra show clear peak of crystalline α-quartz at -107.5 ppm, the spectra of

600 rpm and 800 rpm ball milled SiO_2 show distinct broad peak ranging from -120 ppm to -80 ppm, indicating structure of amorphous SiO_2 possess reduced Q species. These results indicate amorphous structure of SiO_2 increase with increasing mechanical energy, and the short range scale disorder increase with increase of Q^2 and Q^3 species.

3.4. Conclusion

In this study, we explored the detailed structural changes in mechanically amorphized crystalline SiO_2 using Si-29 MAS NMR, and the chemical composition and morphology change using, XRD, EDS-mapping and HR-TEM. Si-29 MAS NMR spectra show the increase of Q^2 and Q^3 species with increased mechanical energy, and along with the XRD pattern, mechanical amorphization occur only when the mechanical energy is stronger than a certain level by sufficient rotational speed. The presence of Q^2 and Q^3 species represents a distinct amorphous structure formed by mechanical amorphization without melting, and implying that chemical reactions are involved in the process of mechanical amorphization. This study provides an understanding of the mechanical amorphization mechanism of SiO_2 and an understanding of atomistic origin of the formation of amorphous SiO_2 layer on fault plane.

REFERENCE

Blaha, P., Schwarz, K., Madsen, G., Kvasnicka, D. and Luitz, J. (2001) wien2k. An augmented plane wave+ local orbitals program for calculating crystal properties.

Di Toro, G., Goldsby, D.L. and Tullis, T.E. (2004) Friction falls towards zero in quartz rock as slip velocity approaches seismic rates. Nature 427, 436-439.

Di Toro, G., Han, R., Hirose, T., De Paola, N., Nielsen, S., Mizoguchi, K., Ferri, F., Cocco, M. and Shimamoto, T. (2011) Fault lubrication during earthquakes. Nature 471, 494-+.

Fukui, H., Kanzaki, M., Hiraoka, N. and Cai, Y.Q. (2009) X-ray Raman scattering for structural investigation of silica/silicate minerals. Physics and Chemistry of Minerals 36, 171-181.

Han, R., Shimamoto, T., Hirose, T., Ree, J.-H. and Ando, J.-i. (2007) Ultralow friction of carbonate faults caused by thermal decomposition. Science 316, 878-881.

Nakamura, Y., Muto, J., Nagahama, H., Shimizu, I., Miura, T. and Arakawa, I. (2012) Amorphization of quartz by friction: Implication to silica-gel lubrication of fault surfaces. Geophysical Research Letters 39.

Kanamori, H., Anderson, D.L. and Heaton, T.H. (1998) Frictional melting during the rupture of the 1994 Bolivian earthquake. Science 279, 839-842.

Kim, H.N. and Lee, S.K. (2013) Atomic structure and dehydration mechanism of amorphous silica: Insights from ^{29}Si and ^{1}H solid-state MAS NMR study of SiO_2 nanoparticles. Geochim. Cosmochim. Ac. 120, 39-64.

Kirkpatrick, J.D., Rowe, C.D., White, J.C. and Brodsky, E.E. (2013) Silica gel formation during fault slip: Evidence from the rock record. Geology 41, 1015-1018.

Kohn, W. and Sham, L.J. (1965) Self-consistent equations including exchange and correlation effects. Physical review 140, A1133.

Kuwayama, Y., Hirose, K., Sata, N. and Ohishi, Y. (2011) Pressure-induced structural evolution of pyrite-type SiO_2. Physics and Chemistry of Minerals 38, 591-597.

Perdew, J.P., Ruzsinszky, A., Csonka, G.I., Vydrov, O.A., Scuseria, G.E., Constantin, L.A., Zhou, X. and Burke, K. (2008) Restoring the density-gradient expansion for exchange in solids and surfaces. Physical Review Letters 100, 136406.

Power, W.L. and Tullis, T.E. (1989) The relationship between slickenside surfaces in fine-grained quartz and the seismic cycle. Journal of Structural Geology 11, 879-893.

Reches, Z.E. and Lockner, D.A. (2010) Fault weakening and earthquake instability by powder lubrication. Nature 467, 452-455.

Schwarz, K. (2003) DFT calculations of solids with LAPW and WIEN2k. Journal of Solid State Chemistry 176, 319-328.

Suryanarayana, C. (2001) Mechanical alloying and milling. Progress in materials science 46, 1-184.

Tse, J.S. (2002) Ab initio molecular dynamics with density functional theory. Annual review of physical chemistry 53, 249-290.

Wu, S., Umemoto, K., Ji, M., Wang, C.Z., Ho, K.M. and Wentzcovitch, R.M. (2011) Identification of post-pyrite phase transitions in SiO_2 by a genetic algorithm. Physical Review B 83, 184102.

4. *AB INITIO* CALCULATIONS OF LOCAL ELECTRONIC STRUCTURES AND X-RAY RAMAN SCATTERING SPECTRA FOR SiO_2 HIGH PRESSURE PHASE

4.1 Introduction

SiO_2 is one of the most abundant oxide components in the Earth and rocky planets and because of its fundamental applications to various chemical components, it also plays an important roles in condensed-matter physics, electronic material engineering, solid-state physics and computational science (Arai et al., 2003; Cohen, 1993; Pirkle et al., 2011; Tsuchiya, 2011; Yonehara et al., 1984). The crystalline SiO_2 undergoes a sequence of phase transitions with changing pressure and temperature (Kuwayama et al., 2011; Wu et al., 2011). The knowledge of electronic structures and physicochemical properties associated with those crystalline phases is essential not only for elucidating the properties of advanced ceramic materials, but also the Earth differentiation from the early stage of bulk silicate melts, the mantle structure of the present Earths and super-Earth with extremely high pressure (Cataldo et al., 2016; Ito et al., 1984; Kuwayama et al., 2011; Nettelmann et al., 2011; Sun, 1987; Tsuchiya et al., 2004; Tsuchiya, 2011; Wu et al., 2011).

The presence of SiO_2 and the formation mechanism of it in the Earth's interior have been proposed from many studies An studies for the Earth structure at the lower mantle conditions reported mid-ocean-ridge basalt (MORB) is composed of 10-20 % amount of free SiO_2, differing from the peridotitic composition (Andrault et al., 2014; Kesson et al., 1994; Ono et al., 2001; Tsuchiya et al., 2004). The other studies also suggested free silica could be also produced as the result of the subducting crust sinks into the deep mantle (Driver et al., 2010; Kesson et al., 1994; Tsuchiya et al., 2004; Vinnik et al., 2001) or the reaction between the bridgmanite of the mantle and the molten Fe of the liquid outer core (Driver et al., 2010; Knittle and Jeanloz, 1991; Tsuchiya et al., 2004). In addition to those studies, the knowledge

of high-pressure SiO_2 polymorphs became more important in seismology and geophysics as the *ab initio* calculation studies suggested the transition condition of stishovite-$CaCl_2$ corresponds to the 1670 km depth where certain seismic anomaly being observed beneath the subduction zone (Andrault et al., 1998; Cordier et al., 2004; Hirose et al., 2005; Kaneshima and Helffrich, 1999; Karki et al., 1997; Kingma et al., 1995), and the transition condition of $CaCl_2$-*a*-PbO_2 corresponds to the depth of D″ layer, close to the core-mantle boundary (Hirose et al., 2005; Knittle and Jeanloz, 1991; Murakami et al., 2003; Tsuchiya et al., 2004).

The pressure-induced structural phases of SiO_2 can be understood by a wide range of atomistic origin studies for their electronic structures. *In situ* x-ray Raman scattering (XRS) uses inelastic hard x-rays to excite electrons near core of atoms and which makes it as one of the powerful methods to investigate local electronic structure of light elements, e.g., Be (Sternemann et al., 2003), B_2O_3 (Lee et al., 2005b), graphite (Mao et al., 2003), and solid oxygen cluster (Meng et al., 2008), and especially under extreme conditions like high pressure (Fukui et al., 2008; Hiraoka and Cai, 2010; Krisch and Sette, 2002). In this regard, the studies for high-pressure induced phase change of SiO_2 using in situ high-pressure XRS became one of the many ways to explore the interior of the Earth (Fukui et al., 2009; Lin et al., 2007; Yi and Lee, 2012a, 2016).

However, the current *in situ* high-pressure XRS studies cannot be extended above ~70 GPa because of the experimental limitation stems from the x-ray beam size, the sample amount, and the scattering geometry in a diamond anvil cell. For the further high pressure XRS studies, overcoming those experimental limitations, *ab initio* calculations based on density functional theory (DFT) have been used in many studies (Wu et al., 2012; Yi and Lee, 2012a). Nevertheless the detailed atomistic origins of O *K*-edge XRS spectrum is still not clear.

Aiming to extend the studies on O *K*-edge XRS studies for SiO_2 and clarify the link between spectral features and detailed origins, here, we calculated the O *K*-edge XRS spectra for nine crystalline SiO_2 polymorphs(*a*-quartz, *β*-quartz, *a*-cristobalite, coesite, hp-cristobalite, penta-SiO_2, stishovite, $CaCl_2$-type, pyrite-type) using WIEN2k program package based on the full-potential linearized augmented plane wave (FP-LAPW) method. We also calculated the radial distribution functions and the partial densities of states (PDOS) of electrons for both ground state and excited state. The calculated spectra of XRS and PDOS allow further understanding on electronic structure of silica polymorphs under ultra-high pressure.

4.2 *Ab initio* calculations

4.2.1 Crystal structures

Calculated crystalline structure of SiO_2 polymorphs were obtained from previous experiments and theoretical studies [*a*-quartz(Will et al., 1988), *β*-quartz(Kihara, 1990), coesite(Levien and Prewitt, 1981), *a*-cristobalite(Schmahl et al., 1992), hp-cristobalite(Huang et al., 2006), penta-SiO_2(Badro et al., 1997), stishovite(Yamanaka et al., 2002), $CaCl_2$-type(Andrault et al., 1998), pyrite-type(Kuwayama et al., 2005)]. Detailed structures of SiO_2 polymorphs used in this studies are listed in Table 1. Four of the nine crystalline SiO_2 polymorphs (which are relatively low-pressure polymorphs than the others), *a*-quartz, *β*-quartz, coesite, *a*-cristobalite and hp-cristobalite consist of SiO_4 tetrahedron as their building units of crystal and only corner sharing oxygen exist. The structure of coesite is especially different from those SiO_4 unit polymorphs. The Si atoms in coesite consist of two crystallographically inequivalent sites (Si1 and Si2), and the O atoms have five sites with different rates (O1:O2:O3:O4:O5 = 1:1:2:2:2). One of the nine crystalline SiO_2 polymorphs,

penta-SiO_2 is induced by deviatoric stresses (nonhydrostatic pressure, 27 GPa along the *c* axis and 20 GPa in the *a, b* plane) and consist of SiO_5 polyhedral which has five coordinated Si atoms. The O atoms in penta SiO_2 have two crystallographically inequivalent sites with same rate (O1:O2 = 1:1) but different coordination $^{[2]}O$ (corner sharing) and $^{[3]}O$ (edge sharing). The other three polymorphs, stishovite, $CaCl_2$-type and pyrite-type consist of SiO_6 octahedron as their building unit with six coordinated Si and every O atoms are three coordinated($^{[3]}O$).

4.2.2 Calculation conditions

In this study we used the WIEN2k as calculation program package based on the full-potential linearized augmented plane wave+local orbitals (FP-LAPW+lo) method(Blaha et al., 2001). Unlike some other calculation methods consider only valence electrons, FP-LAPW+lo method describes all the electronic states of an atom by classifying into three regions (core states, valence states and semi core state), and which make it become as a one of the most powerful methods to calculate core-level spectroscopy. The Perdew-Berke-Ernzerhof for the solid (PBESOL) based on the generalized gradient approximation (GGA) method was used as the exchange-correlation functional to describe the short-range electronic interactions (Perdew et al., 2008; Yi and Lee, 2012a, 2016). The Muffin-Tin radius (R_{MT}) which decide atomic radius was arranged as ~1.44–1.62 Å, automatically based on atomic distances in unit cell by WIEN2k program. The cutoff energy for separation of core and valence states electron is -6.0 ~ -7.1 Ry (1 Ry = 13.6 eV), and -7.1 Ry threshold including the Si 2*p*-orbital as a valence state during self-consistent field (SCF) calculations prevents potential leakage of core electrons from the M-T sphere. The largest vector in the Fourier expansion of charge density (G_{MAX}) was set to 14.0. To calculate the electronic structure of SiO_2 polymorphs we used the number of inequivalent *k*-points in the irreducible Brillouin

zone range 8~48, depending on the number of atoms in each unit cell. The SCF calculations were carried out using the convergence criteria of 10^{-4} Ry for the total energy and 10^{-3} e for the charge (Yi and Lee, 2012a, 2016) .

4.2.3 PDOS and O *K*-edge XRS calculations

The both ground state and excited state PDOS for each orbital of the atoms were calculated to analyze the O *K*-edge XRS spectra and electronic structure of SiO_2 polymorphs. The PDOS for ground state SiO_2 phases were performed with unit cell structures, without any modification for electronic structure and calculated for each crystallographically inequivalent atoms as well as the PDOS for the total electronic structure. The excited state PDOS and O *K*-edge XRS calculation for SiO_2 polymorphs were performed with super cell structure, expanding the original unit cell in three dimensions, and modified the 1s orbital electron of specific one O atoms for each SiO_2 polymorphs, to describe the excited state O atom. Also, the excited state PDOS and O *K*-edge XRS were calculated for each crystallographically inequivalent oxygen site, which has excited 1s electron, in the crystals to investigate the link between spectral features and atomistic origins, considering their existence rates (coesite O1:O2:O3:O4:O5 = 1:1:2:2:2, penta-SiO_2 O1:O2 = 1:1, in case of excited state PDOS crystallographically inequivalent silicon sites in coesite also calculated, Si1:Si2 = 1:1).

The ground-state PDOS calculations are presented in the range of -30 to 30 eV, while the excited state PDOS calculations are 0 to 30 eV, and each spectrum is presented with the full-width at half maximum (FWHM) Gaussian broadening factor of 0.005 eV. The O *K*-edge calculations used binding energy of ~538.25 eV, and considered both dipole transition and multiple transition, and FWHM Gaussian broadening factor of 0.005 eV and are presented in the energy range of 0 to 30 eV.

4.3 Results and Discussion

4.3.1 O *K*-edge x-ray Raman scattering

Figure 7 (a) shows O *K*-edge XRS spectra of coesite for each crystallographically inequivalent oxygen sites (black solid) and total O *K*-edge XRS spectrum (red solid). The total oxygen coesite O *K*-edge XRS feature are similar to those of *a*-quartz, these features are known to stems from the excitation of 1s-state core electron of oxygen into the *sp*-hybridized state between the oxygen 2*p*-state and the silicon 3*s*- and 3*p*-state (Yi and Lee, 2012b). The O *K*-edge XRS spectra of coesite were calculated with their existence rates of five crystallographically distinct oxygen sites, which are only consist of bridging oxygen. Although those five crystallographically distinct corner-sharing oxygen have same Si coordination and in the same crystal unit, each O *K*-edge XRS spectrum features are quite different in the energy range above 11 eV, and this result suggest that the energy range above the ~11 eV represent the crystallographic structural variations like bond angels and bond lengths ($^{[4]}$Si-$^{[2]}$O-$^{[4]}$Si and Si-O).

Figure 7 (b) shows O *K*-edge XRS spectra of penta-SiO_2 for each crystallographically inequivalent oxygen sites (black solid) and total O *K*-edge XRS spectrum (red solid). The calculated total O *K*-edge XRS spectrum for penta-SiO_2 (red solid) shows apparent double peaks. O *K*-edge XRS spectrum of each crystallographically inequivalent oxygen shows quit similar spectral features regarding their coordination difference between O1 ($^{[3]}$O) and O2($^{[2]}$O). This result suggest important standard of analysis to O *K*-edge XRS spectrum, representing the coordination of oxygen is not an impactful factor.

Figure 7 (c) shows the total O *K*-edge XRS spectra of SiO_2 high pressure phases. Except the O *K*-edge XRS spectrum of hp-cristobalite, all SiO_4 tetrahedral based crystal structure with $^{[4]}$Si present a dominant feature at ~8.7 eV. While the dominant feature at ~8.7

eV is shown as common spectral feature for *a*-quartz, *β*-quartz, *a*-cristobalite, and coesite, small features above ~11 eV are differ with crystal structure. In this regard, the results of small features above ~11 eV imply that these features stem from crystalline structure. On the other hand, the O *K*-edge XRS spectrum of hp-cristobalite, showing clear double peaks, is much more similar to that of the penta-SiO_2 or stishovite, consisting of $^{[5]}$Si and $^{[6]}$Si respectively. While other previous studies suggested that spectral difference of O *K*-edge XRS could arise from coordination of silicon(Lin et al., 2007), this result prove that the spectral features of O *K*-edge XRS are independent with the silicon coordination.

4.3.2 Correlation between spectrum and crystal structure

Figure 7 (a) shows O *K*-edge XRS spectra of coesite for each crystallographically inequivalent oxygen sites (black solid) and total O *K*-edge XRS spectrum (red solid). The total oxygen coesite O *K*-edge XRS feature are similar to those of *a*-quartz, these features are known to stems from the excitation of 1s-state core electron of oxygen into the sp-hybridized state between the oxygen 2*p*-state and the silicon 3*s*- and 3*p*-state (Yi and Lee, 2012b). The O *K*-edge XRS spectra of coesite were calculated with their existence rates of five crystallographically distinct oxygen sites, which are only consist of bridging oxygen. Although those five crystallographically distinct corner-sharing oxygen have same Si coordination and in the same crystal unit, each O *K*-edge XRS spectrum features are quite different in the energy range above 11 eV, and this result suggest that the energy range above the ~11 eV represent the crystallographic structural variations like bond angels and bond lengths ($^{[4]}$Si-$^{[2]}$O-$^{[4]}$Si and Si-O).

Figure 7 (b) shows O *K*-edge XRS spectra of penta-SiO_2 for each crystallographically inequivalent oxygen sites (black solid) and total O *K*-edge XRS spectrum (red solid). The calculated total O *K*-edge XRS spectrum for penta-SiO_2 (red solid) shows apparent double

peaks. O *K*-edge XRS spectrum of each crystallographically inequivalent oxygen shows quit similar spectral features regarding their coordination difference between O1 ($^{[3]}$O) and O2($^{[2]}$O). This result suggest important standard of analysis to O *K*-edge XRS spectrum, representing the coordination of oxygen is not an impactful factor.

Figure 7 (c) shows the total O *K*-edge XRS spectra of SiO_2 high pressure phases. Except the O *K*-edge XRS spectrum of hp-cristobalite, all SiO_4 tetrahedral based crystal structure with $^{[4]}$Si present a dominant feature at ~8.7 eV. While the dominant feature at ~8.7 eV is shown as common spectral feature for *α*-quartz, *β*-quartz, *α*-cristobalite, and coesite, small features above ~11 eV are differ with crystal structure. In this regard, the results of small features above ~11 eV imply that these features stem from crystalline structure. On the other hand, the O *K*-edge XRS spectrum of hp-cristobalite, showing clear double peaks, is much more similar to that of the penta-SiO_2 or stishovite, consisting of $^{[5]}$Si and $^{[6]}$Si respectively. While other previous studies suggested that spectral difference of O *K*-edge XRS could arise from coordination of silicon(Lin et al., 2007), this result prove that the spectral features of O *K*-edge XRS are independent with the silicon coordination.

4.4 Conclusion

In this study, we report the electronic structure of various SiO_2 polymorphs and detailed origin of the O *K*-edge XRS features for SiO_2 polymorphs, and provide the clear link with the crystal structures, using WIEN2k program package. The O *K*-edge XRS of hp-cristobalite and penta-SiO_2 show clear double peak shape which is similar with that of the stishovite, six coordinated Si crystal, and prove that there is no direct relation between Si coordination and the spectral features. Also the O *K*-edge XRS penta-SiO_2 for crystallographically site resolved oxygen (O1 and O2) show similar shape, and prove that there is no direct relation between O coordination and the spectral features either. In other

hand, the change of spectral features of O *K*-edge XRS has clear relation with the O-O distance, crystal SiO_2 with double peak shape O *K*-edge XRS possess O-O distance shorter than ~2.54 Å. This results indicate that the formation of 2*p*-hybridzation between oxygen orbital may induce the O *K*-edge XRS spectral change.

REFERENCE

Andrault, D., Fiquet, G., Guyot, F. and Hanfland, M. (1998) Pressure-induced Landau-type transition in stishovite. Science 282, 720-724.

Andrault, D., Pesce, G., Bouhifd, M.A., Casanova, B.N., Hénot, J.M. and Mezouar, M. (2014) Melting of subducted basalt at the core-mantle boundary. Science 344, 892-895.

Arai, S., Shimizu, Y. and Gervilla, F. (2003) Quartz diorite veins in a peridotite xenolith from Tallante, Spain: implications for reaction and survival of slab-derived SiO_2-oversaturated melt in the upper mantle. Proceedings of the Japan Academy, Series B 79, 145-150.

Badro, J., Teter, D.M., Downs, R.T., Gillet, P., Hemley, R.J. and Barrat, J.L. (1997) Theoretical study of a five-coordinated silica polymorph. Physical Review B 56, 5797.

Cataldo, G.F., Davis, S. and Gutiérrez, G. (2016) Z method calculations to determine the melting curve of silica at high pressures. J. Phys. Conf. Ser. 720, 012032.

Cohen, R.E. (1993) First-principles predictions of elasticity and phase transitions in high pressure SiO_2 and geophysical implications. High-pressure research: Application to earth and planetary sciences, 425-431.

Cordier, P., Mainprice, D. and Mosenfelder, J.L. (2004) Mechanical instability near the stishovite-$CaCl_2$ phase transition. European journal of mineralogy 16, 387-399.

De La Pierre, M., Orlando, R., Maschio, L., Doll, K., Ugliengo, P. and Dovesi, R. (2011) Performance of six functionals (LDA, PBE, PBESOL, B3LYP, PBE0, and WC1LYP) in the simulation of vibrational and dielectric properties of crystalline compounds. The case of forsterite Mg_2SiO_4. Journal of computational chemistry 32, 1775-1784.

Driver, K.P., Cohen, R.E., Wu, Z., Militzer, B., Ríos, P.L., Towler, M.D., Needs, R.J. and Wilkins, J.W. (2010) Quantum Monte Carlo computations of phase stability, equations of state, and elasticity of high-pressure silica. Proceedings of the National Academy of Sciences 107, 9519-9524.

Fukui, H., Kanzaki, M., Hiraoka, N. and Cai, Y.Q. (2008) Coordination environment of silicon in silica glass up to 74 GPa: An x-ray Raman scattering study at the silicon L edge. Physical Review B 78, 012203.

Hiraoka, N. and Cai, Y.Q. (2010) High-pressure studies by x-ray Raman scattering. Synchrotron Radiation News 23, 26-31.

Hirose, K., Takafuji, N., Sata, N. and Ohishi, Y. (2005) Phase transition and density of subducted MORB crust in the lower mantle. Earth and Planetary Science Letters 237, 239-251.

Huang, L., Durandurdu, M. and Kieffer, J. (2006) Transformation pathways of silica under high pressure. Nature materials 5, 977-981.

Ito, E., Takahashi, E. and Matsui, Y. (1984) The mineralogy and chemistry of the lower mantle: an implication of the ultrahigh-pressure phase relations in the system $MgOFeOSiO_2$. Earth and Planetary Science Letters 67, 238-248.

Kaneshima, S. and Helffrich, G. (1999) Dipping low-velocity layer in the mid-lower mantle: evidence for geochemical heterogeneity. Science 283, 1888-1892.

Karki, B.B., Warren, M.C., Stixrude, L., Ackland, G.J. and Crain, J. (1997) Ab initio studies of high-pressure structural transformations in silica. Physical Review B 55, 3465.

Kesson, S.E., Gerald, J.D.F. and Shelley, J.M.G. (1994) Mineral chemistry and density of subducted basaltic crust at lower-mantle pressures. Nature 372, 767-769.

Kihara, K. (1990) An X-ray study of the temperature dependence of the quartz structure. European Journal of Mineralogy, 63-78.

Kingma, K.J., Cohen, R.E., Hemley, R.J. and Mao, H.K. (1995) Transformation of stishovite to a denser phase at lower-mantle pressures. Nature 374, 243-245.

Knittle, E. and Jeanloz, R. (1991) Earth's core-mantle boundary: results of experiments at high pressures and temperatures. Science 251, 1438.

Krisch, M. and Sette, F. (2002) X-ray Raman scattering from low Z materials. Surface Review and Letters 9, 969-976.

Kuwayama, Y., Hirose, K., Sata, N. and Ohishi, Y. (2005) The pyrite-type high-pressure form of silica. Science 309, 923-925.

Lee, S.K., Eng, P.J., Mao, H.K., Meng, Y., Newville, M., Hu, M.Y. and Shu, J. (2005b) Probing of bonding changes in B_2O_3 glasses at high pressure with inelastic x-ray scattering. Nature Materials 4, 851-854.

Levien, L. and Prewitt, C.T. (1981) High-pressure crystal structure and compressibility of coesite.

Lin, J.F., Fukui, H., Prendergast, D., Okuchi, T., Cai, Y.Q., Hiraoka, N., Yoo, C.S., Trave, A., Eng, P. and Hu, M.Y. (2007) Electronic bonding transition in compressed SiO 2 glass. Physical Review B 75, 012201.

Mao, W.L., Mao, H.K., Eng, P.J., Trainor, T.P., Newville, M., Kao, C.C., Heinz, D.L., Shu, J., Meng, Y. and Hemley, R.J. (2003) Bonding changes in compressed superhard graphite. Science 302, 425-427.

Meng, Y., Eng, P.J., John, S.T., Shaw, D.M., Hu, M.Y., Shu, J., Gramsch, S.A., Kao, C.C., Hemley, R.J. and Mao, H.K. (2008) Inelastic x-ray scattering of dense solid oxygen: Evidence for intermolecular bonding. Proceedings of the National Academy of Sciences 105, 11640-11644.

Murakami, M., Hirose, K., Ono, S. and Ohishi, Y. (2003) Stability of $CaCl_2$-type and α-PbO_2-type SiO_2 at high pressure and temperature determined by in-situ X-ray measurements. Geophysical Research Letters 30.

Nettelmann, N., Fortney, J.J., Kramm, U. and Redmer, R. (2011) Thermal evolution and structure models of the transiting super-Earth GJ 1214b. The Astrophysical Journal 733, 2.

Ono, S., Ito, E. and Katsura, T. (2001) Mineralogy of subducted basaltic crust (MORB) from 25 to 37 GPa, and chemical heterogeneity of the lower mantle. Earth and Planetary Science Letters 190, 57-63.

Pirkle, A., Chan, J., Venugopal, A., Hinojos, D., Magnuson, C.W., McDonnell, S., Colombo, L., Vogel, E.M., Ruoff, R.S. and Wallace, R.M. (2011) The effect of chemical residues on the physical and electrical properties of chemical vapor deposited graphene transferred to SiO_2. Applied Physics Letters 99, 122108.

Schmahl, W.W., Swainson, I.P., Dove, M.T. and Graeme-Barber, A. (1992) Landau free energy and order parameter behaviour of the α/β phase transition in cristobalite. Zeitschrift für Kristallographie-Crystalline Materials 201, 125-146.

Sternemann, C., Volmer, M., Soininen, J.A., Nagasawa, H., Paulus, M., Enkisch, H., Schmidt, G., Tolan, M. and Schülke, W. (2003) Momentum-transfer dependence of x-ray Raman scattering at the Be K-edge. Physical Review B 68, 035111.

Sun, S.S. (1987) Chemical composition of Archaean komatiites: implications for early history of the earth and mantle evolution. Journal of volcanology and geothermal research 32, 67-82.

Tsuchiya, T., Caracas, R. and Tsuchiya, J. (2004) First principles determination of the phase boundaries of high-pressure polymorphs of silica. Geophysical Research Letters 31.

Tsuchiya, T.a.T., J. (2011) Prediction of a hexagonal SiO_2 phase affecting stabilities of $MgSiO_3$ and $CaSiO_3$ at multimegabar pressures. Proceedings of the National Academy of Sciences 108, 1252-1255.

Vinnik, L., Kato, M. and Kawakatsu, H. (2001) Search for seismic discontinuities in the lower mantle. Geophysical Journal International 147, 41-56.

Will, G., Bellotto, M., Parrish, W. and Hart, M. (1988) Crystal structures of quartz and magnesium germanate by profile analysis of synchrotron-radiation high-resolution powder data. Journal of Applied Crystallography 21, 182-191.

Wu, M., Liang, Y.F., Jiang, J.Z. and John, S.T. (2012) Structure and properties of dense silica glass. Scientific reports 2.

Yamanaka, T., Fukuda, T. and Mimaki, J. (2002) Bonding character of SiO2 stishovite under high pressures up to 30 GPa. Physics and chemistry of minerals 29, 633-641.

Yi, Y.S. and Lee, S.K. (2012a) Pressure-induced changes in local electronic structures of SiO_2 and $MgSiO_3$ polymorphs: Insights from ab initio calculations of O K-edge energy-loss near-edge structure spectroscopy. American Mineralogist 97, 897-909.

Yi, Y.S. and Lee, S.K. (2012b) Pressure-induced changes in local electronic structures of SiO_2 and $MgSiO_3$ polymorphs: Insights from ab initio calculations of O K-edge energy-loss near-edge structure spectroscopy. Am. Mineral. 97, 897-909.

Yi, Y.S. and Lee, S.K. (2016) Atomistic origins of pressure-induced changes in the O K-edge x-ray Raman scattering features of Si O_2 and MgSi O_3 polymorphs: Insights from ab initio calculations. Physical Review B 94, 094110.

Yonehara, T., Smith, H.I., Thompson, C.V. and Palmer, J.E. (1984) Graphoepitaxy of Ge on SiO_2 by solid-state surface-energy-driven grain growth. Applied Physics Letters 45, 631-633.

TABLES

Name	α-quartz[a]	β-quartz[b]	α-cristobalite[c]	coesite[d]	hp-cristobalite[e]	penta-SiO_2[f]	stishovite[g]	$CaCl_2$-type[h]	pyrite-type[i]
Si coordinate			$^{[4]}$Si			$^{[5]}$Si		$^{[6]}$Si	
System	Trigonal	Hexagonal	Tetragonal	Monoclinic	Tetragonal	Trigonal	Tetragonal	Orthorhombic	Cubic
Space Group	$P3_121$	$P6_222$	$P4_12_12$	C2/c	$P4_12_12$	$P3_221$	$P4_2/mnm$	$Pnnm$	$Pa3$
Cell parameter (Å)									
a	4.912	4.997	4.969	7.136	4.355	4.414	4.181	3.897	3.923
b	4.912	4.997	4.969	12.369	4.355	4.414	4.181	4.001	3.923
c	5.404	5.457	6.926	7.174	5.960	9.358	2.666	2.566	3.923
Si-O bond length (Å)									
Avg. Si-O	1.608	1.588	1.604	1.611	1.554	1.703	1.775	1.694	1.605
O-O distances (Å)									
Avg. O-O	2.626	2.593	2.618	2.630	2.522	2.593	2.509	2.394	2.264
Si-O-Si bond angles									
Avg. Si-O-Si	143.72	153.28	146.38	-	135.07	134.74	130.67	130.00	119.59
Polyhedral volume ($Å^3$)	2.1339	2.0531	2.1145	2.1433	1.8484	3.9297	7.3736	6.4105	5.3380
Crystal densities (g/cm^3)									
ρ	2.65	2.54	2.33	2.92	3.53	3.79	4.28	4.99	6.61

FIGURE

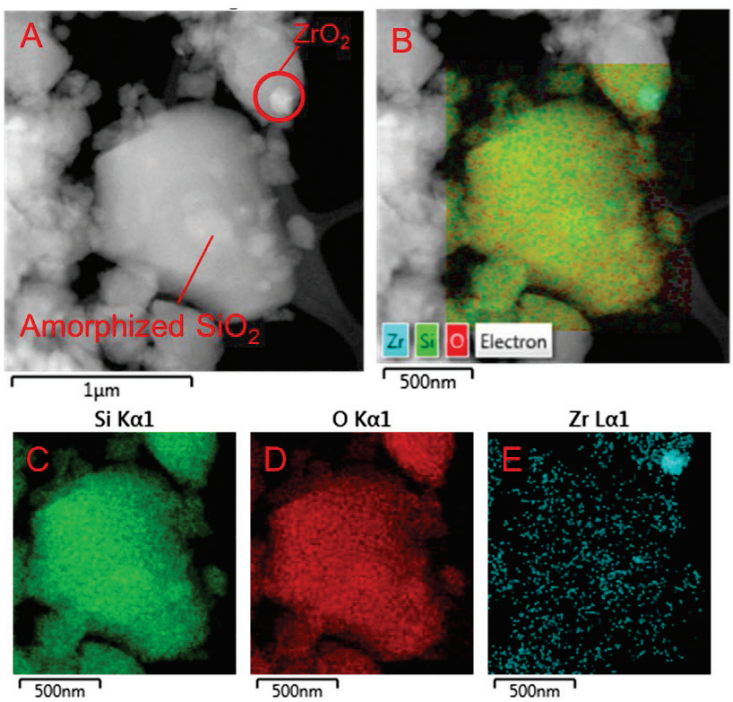

Figure 1

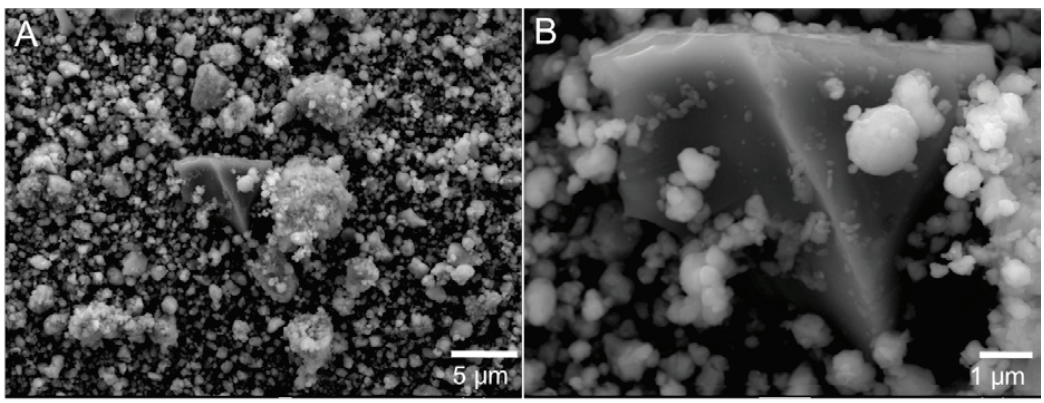

Figure 2

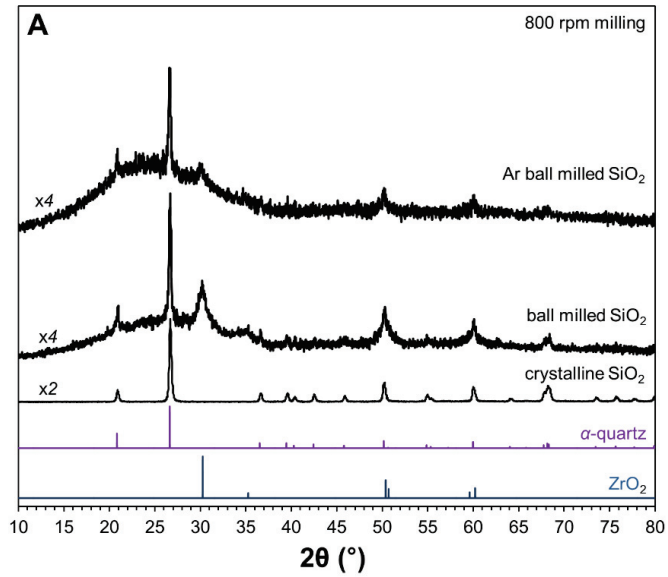
A
800 rpm milling
Ar ball milled SiO2
x4
ball milled SiO2
x4
crystalline SiO2
x2
α-quartz
ZrO2
10 15 20 25 30 35 40 45 50 55 60 65 70 75 80
2θ (°)

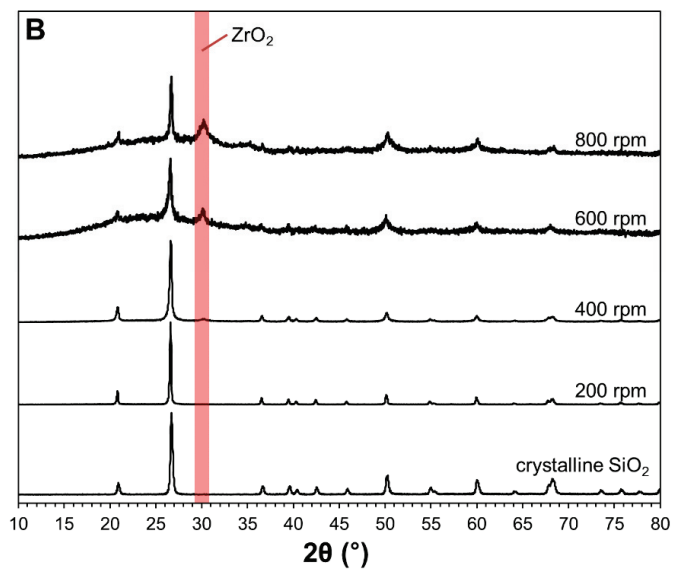
B
ZrO2
800 rpm
600 rpm
400 rpm
200 rpm
crystalline SiO2
10 15 20 25 30 35 40 45 50 55 60 65 70 75 80
2θ (°)

Figure 3

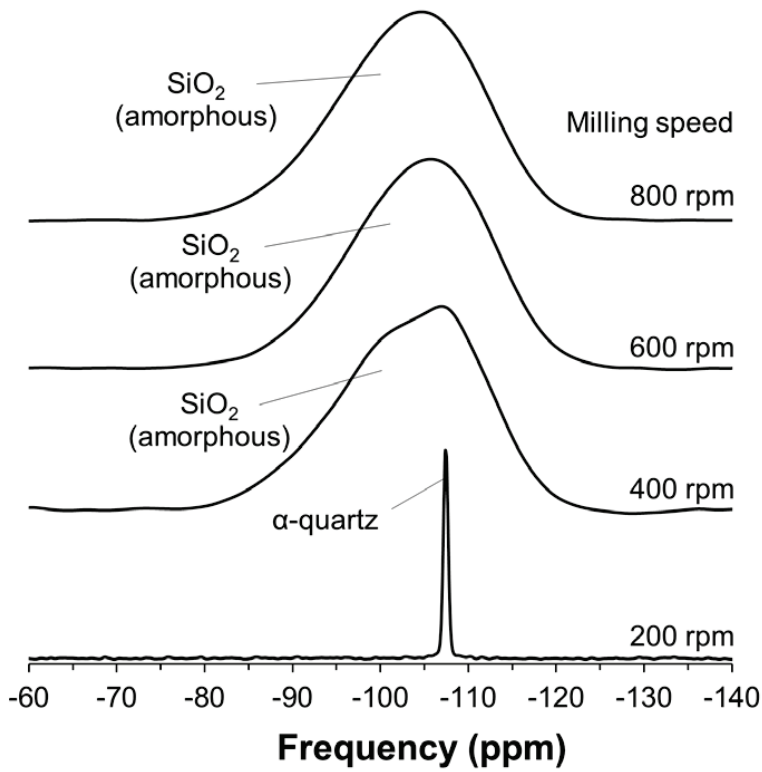
SiO2
(amorphous)
Milling speed
800 rpm
SiO2
(amorphous)
600 rpm
SiO2
(amorphous)
400 rpm
α-quartz
200 rpm
-60
-70
-80
-90
-100
-110
-120
-130
-140
Frequency (ppm)

Figure 4

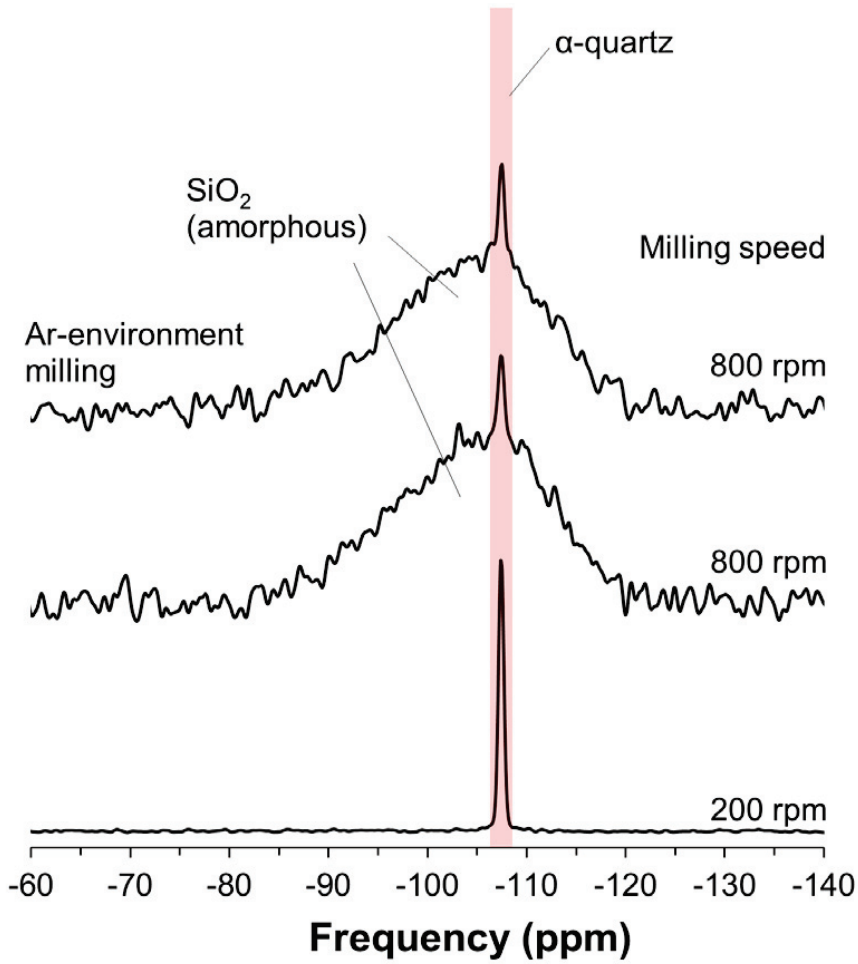
α-quartz
SiO2
(amorphous)
Milling speed
Ar-environment
milling
800 rpm
800 rpm
200 rpm
-60
-70
-80
-90
-100
-110
-120
-130
-140
Frequency (ppm)

Figure 5

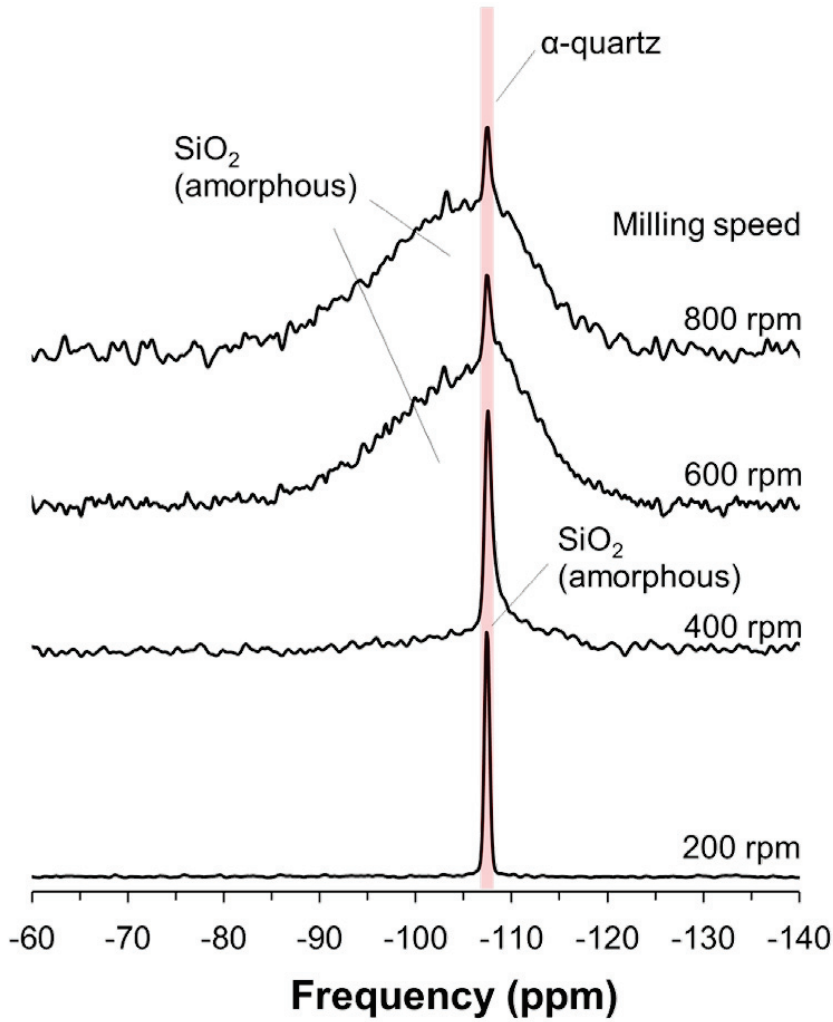
α-quartz
SiO2
(amorphous)
Milling speed
800 rpm
600 rpm
SiO2
(amorphous)
400 rpm
200 rpm
-60
-70
-80
-90
-100
-110
-120
-130
-140
Frequency (ppm)

Figure 6

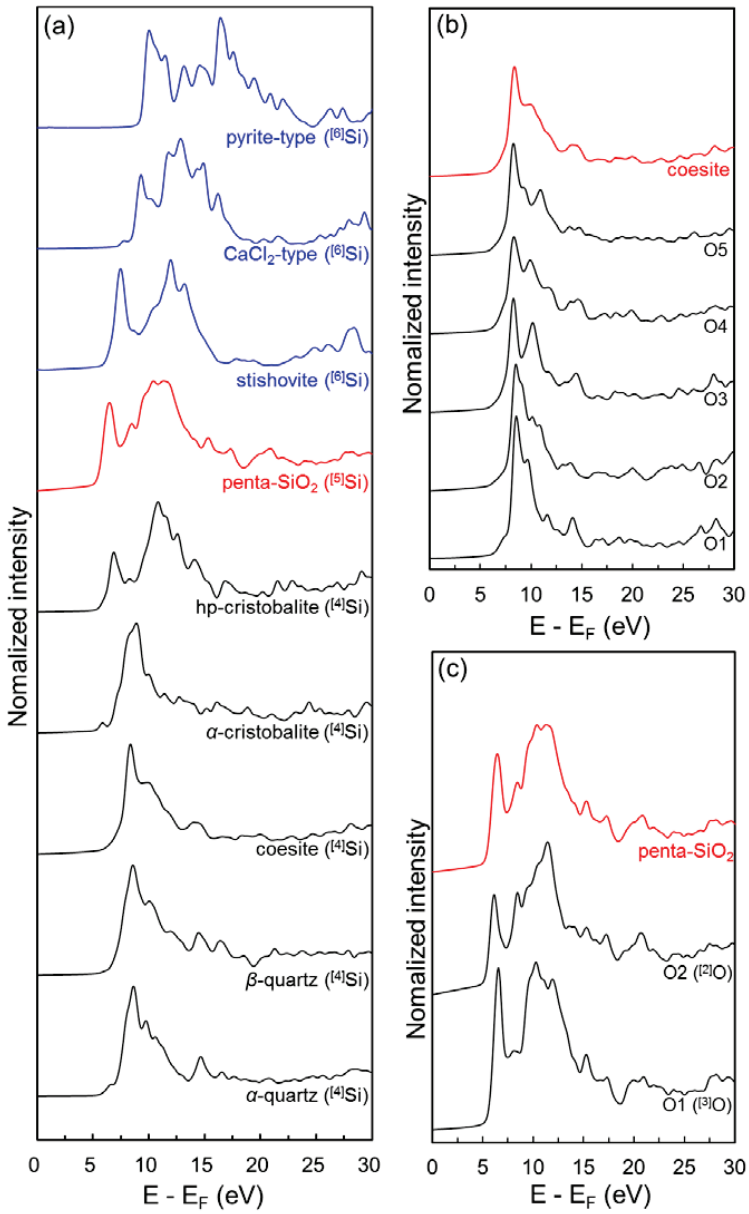
(a)
pyrite-type ([6]Si)
CaCl2-type ([6]Si)
stishovite ([6]Si)
penta-SiO2 ([5]Si)
hp-cristobalite ([4]Si)
α-cristobalite ([4]Si)
coesite ([4]Si)
β-quartz ([4]Si)
α-quartz ([4]Si)
Nomalized intensity
0 5 10 15 20 25 30
E - EF (eV)
(b)
coesite
O5
O4
O3
O2
O1
Nomalized intensity
0 5 10 15 20 25 30
E - EF (eV)
(c)
penta-SiO2
O2 ([2]O)
O1 ([3]O)
Nomalized intensity
0 5 10 15 20 25 30
E - EF (eV)

Figure 7

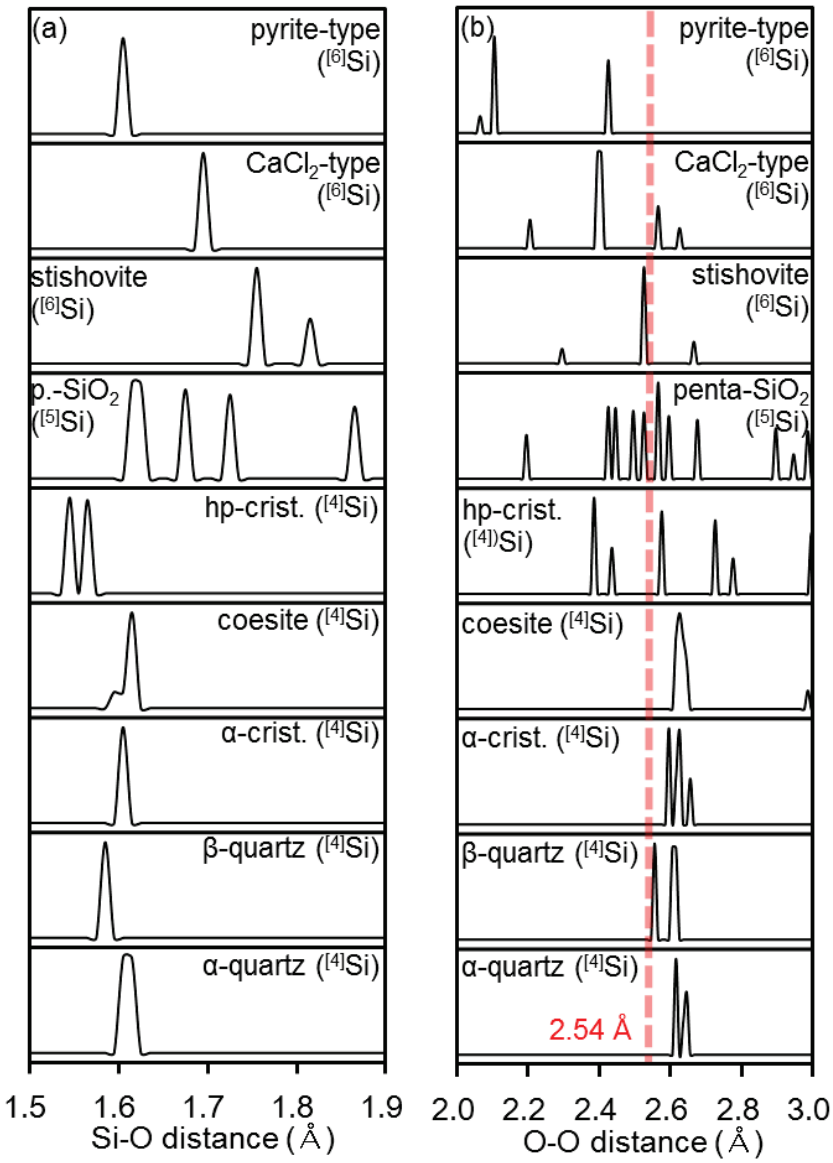
(a)
pyrite-type ([6]Si)
CaCl2-type ([6]Si)
stishovite ([6]Si)
p.-SiO2 ([5]Si)
hp-crist. ([4]Si)
coesite ([4]Si)
α-crist. ([4]Si)
β-quartz ([4]Si)
α-quartz ([4]Si)
1.5 1.6 1.7 1.8 1.9
Si-O distance (Å)
(b)
pyrite-type ([6]Si)
CaCl2-type ([6]Si)
stishovite ([6]Si)
penta-SiO2 ([5]Si)
hp-crist. ([4])Si)
coesite ([4]Si)
α-crist. ([4]Si)
β-quartz ([4]Si)
α-quartz ([4]Si)
2.54 Å
2.0 2.2 2.4 2.6 2.8 3.0
O-O distance (Å)

Figure 8

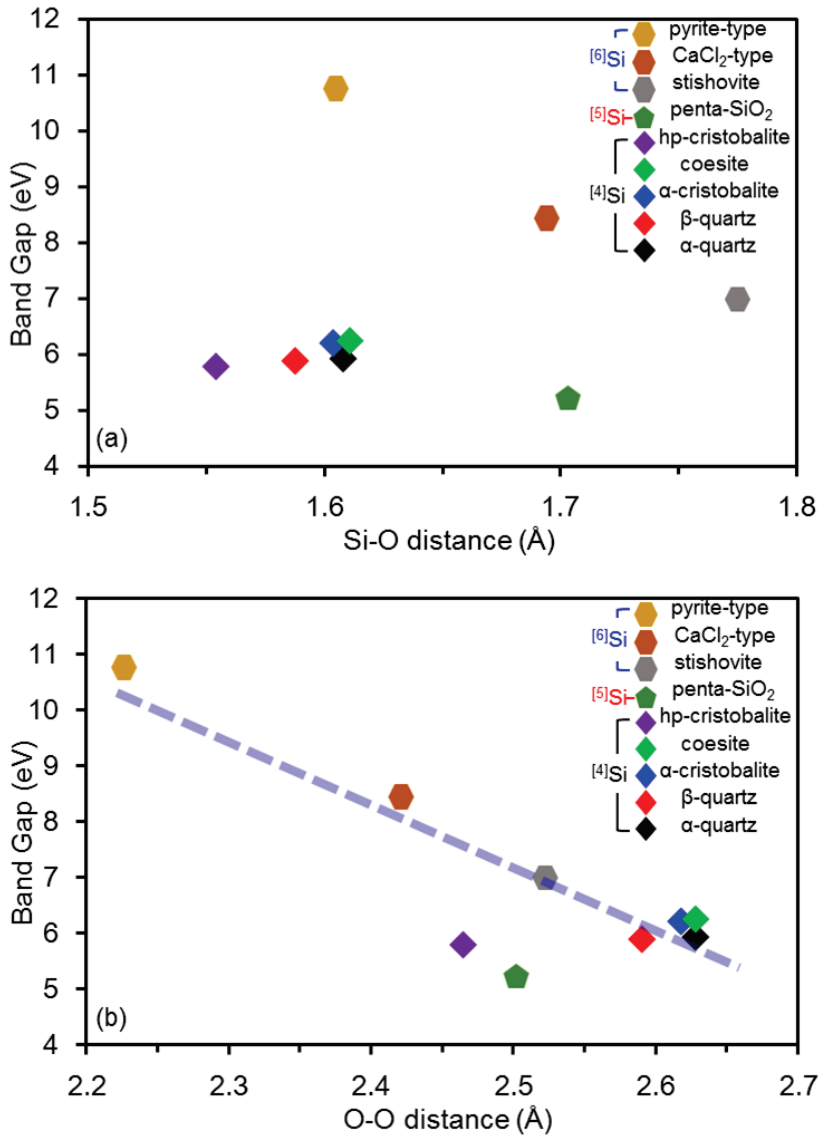
Band Gap (eV)
Si-O distance (Å)
(a)
O-O distance (Å)
(b)
pyrite-type
[6]Si
CaCl2-type
stishovite
[5]Si
penta-SiO2
hp-cristobalite
coesite
[4]Si
α-cristobalite
β-quartz
α-quartz

Figure 9

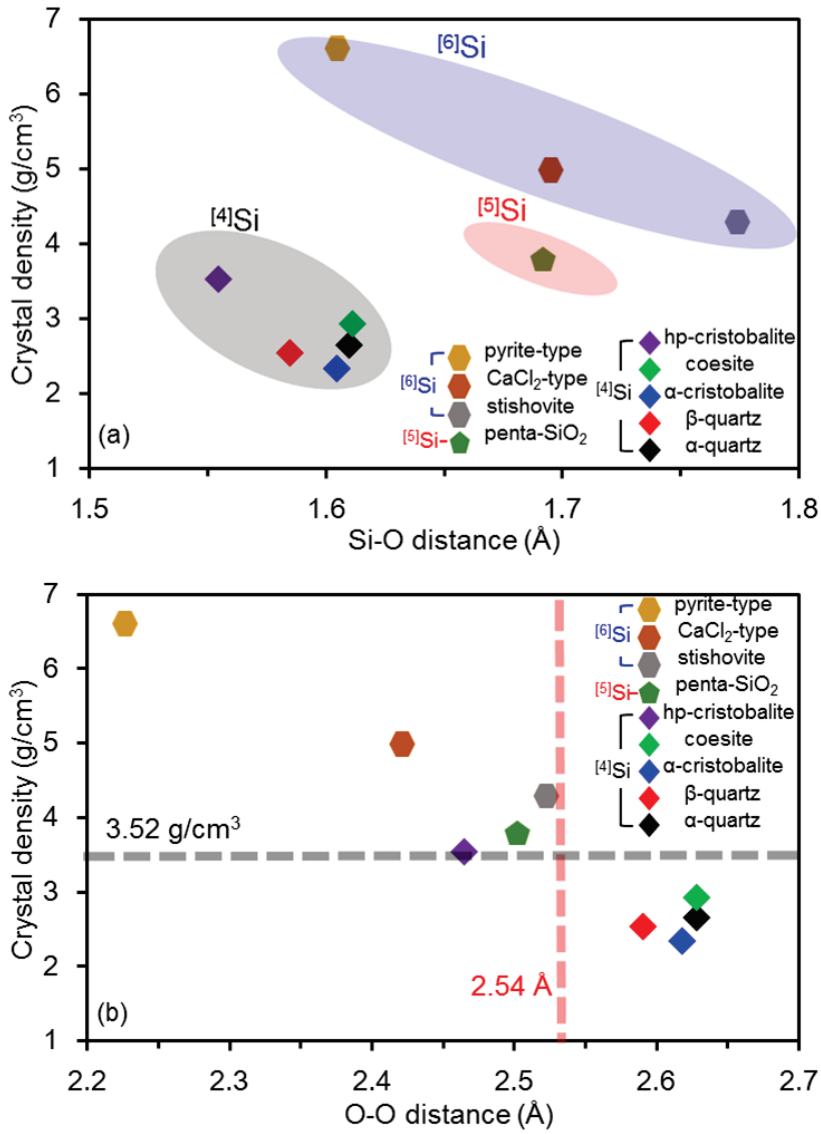
[6]Si
[5]Si
[4]Si
pyrite-type
CaCl2-type
stishovite
penta-SiO2
hp-cristobalite
coesite
α-cristobalite
β-quartz
α-quartz
(a)
Crystal density (g/cm3)
Si-O distance (Å)
3.52 g/cm3
2.54 Å
(b)
O-O distance (Å)

Figure 10

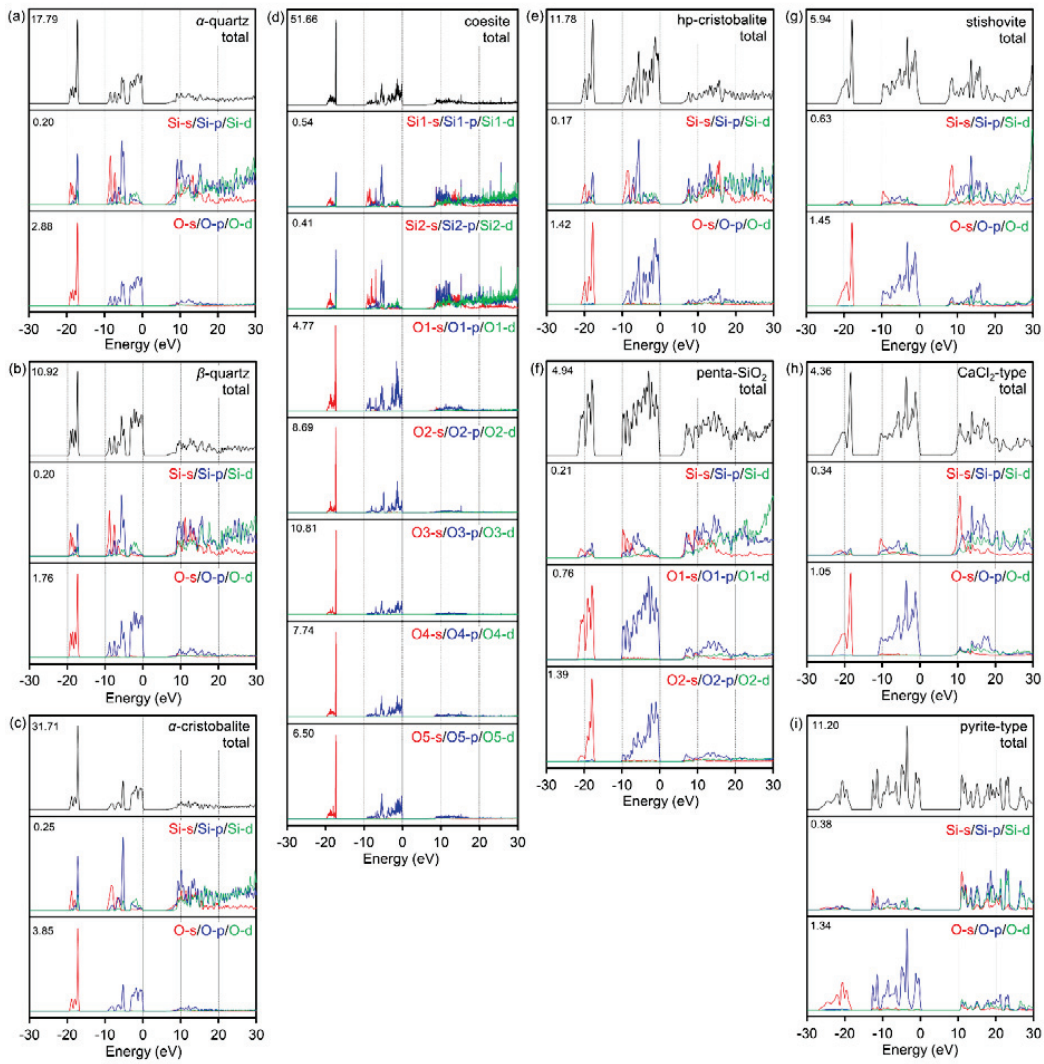
(a)
α-quartz
total
Si-s/Si-p/Si-d
O-s/O-p/O-d
(b)
β-quartz
total
Si-s/Si-p/Si-d
O-s/O-p/O-d
(c)
α-cristobalite
total
Si-s/Si-p/Si-d
O-s/O-p/O-d
(d)
coesite
total
Si1-s/Si1-p/Si1-d
Si2-s/Si2-p/Si2-d
O1-s/O1-p/O1-d
O2-s/O2-p/O2-d
O3-s/O3-p/O3-d
O4-s/O4-p/O4-d
O5-s/O5-p/O5-d
(e)
hp-cristobalite
total
Si-s/Si-p/Si-d
O-s/O-p/O-d
(f)
penta-SiO2
total
Si-s/Si-p/Si-d
O1-s/O1-p/O1-d
O2-s/O2-p/O2-d
(g)
stishovite
total
Si-s/Si-p/Si-d
O-s/O-p/O-d
(h)
CaCl2-type
total
Si-s/Si-p/Si-d
O-s/O-p/O-d
(i)
pyrite-type
total
Si-s/Si-p/Si-d
O-s/O-p/O-d
Energy (eV)

Figure A1

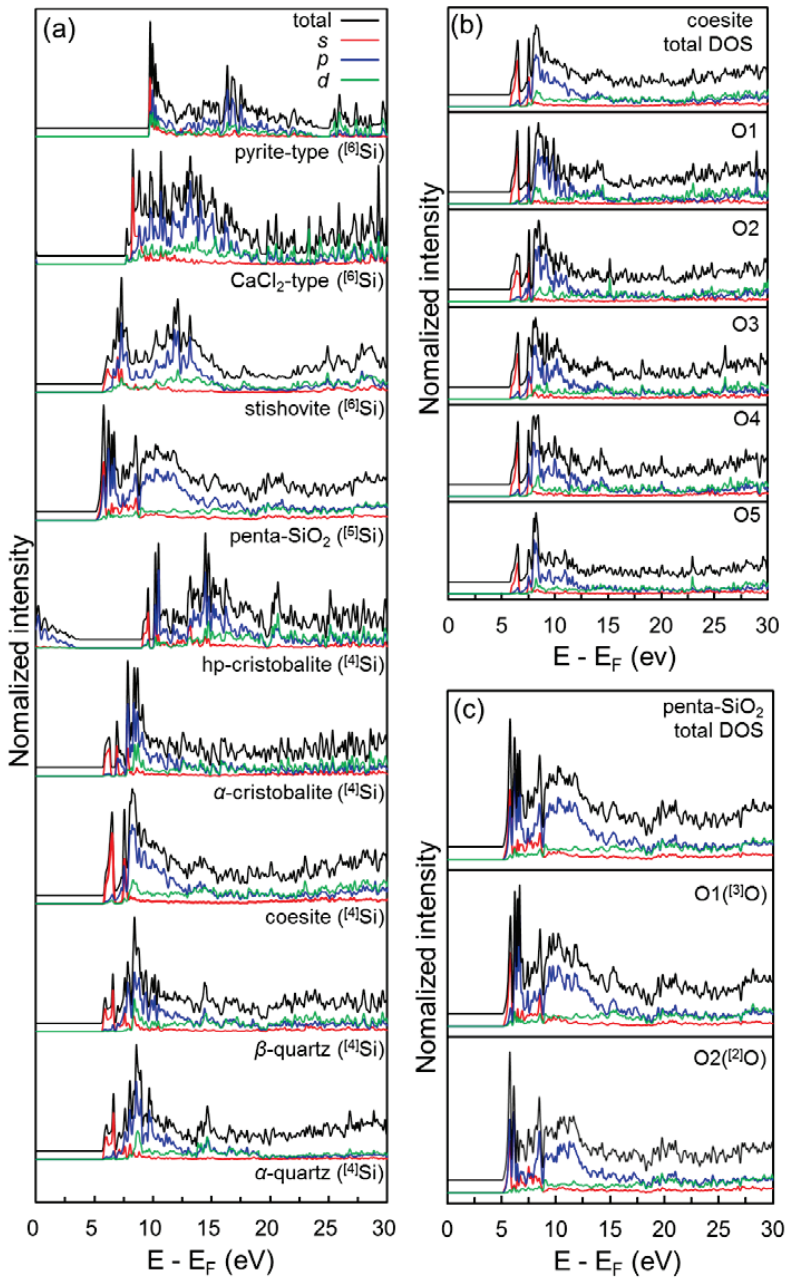
(a)
total
s
p
d
pyrite-type ([6]Si)
CaCl2-type ([6]Si)
stishovite ([6]Si)
penta-SiO2 ([5]Si)
hp-cristobalite ([4]Si)
α-cristobalite ([4]Si)
coesite ([4]Si)
β-quartz ([4]Si)
α-quartz ([4]Si)
Nomalized intensity
0 5 10 15 20 25 30
E - EF (eV)
(b)
coesite
total DOS
O1
O2
O3
O4
O5
Nomalized intensity
0 5 10 15 20 25 30
E - EF (ev)
(c)
penta-SiO2
total DOS
O1([3]O)
O2([2]O)
Nomalized intensity
0 5 10 15 20 25 30
E - EF (eV)

Figure A2

Appendix section

Appendix I. partial density of state (PDOS) for SiO_2 polymorphs

Figure A2 present the result of calculating the PDOS (for each *s*-, *p*- and *d*- orbital of crystallographically inequivalent atom site) for ground state crystalline SiO_2 polymorphs in the valence band and conduction band regions. O *s*-orbitals intensity decrease with the increasing crystalline density, and show delocalization, broadening of the electron orbitals over a large area, in the valence electron region. On the other hand, O *s*-orbitals intensity relatively increase with increasing crystalline density. The discontinuity of the O *p*-orbital near ~-3.5 eV disappear for those SiO_2 polymorphs, which consist of SiO_5 or SiO_6 polyhedral. This indicate the lone pair electrons in the *2p*-orbital of O atoms form hybridization with the vacant *3d*-orbital of Si atoms and form new electron bonds. Especially, the high-pressure phase crystalline SiO_2, consist of SiO_6 polyhedral, exhibits a high energy region of the conduction band, indicating the pressure-induced shift of conduction band to high energy region. The pyrite-type SiO_2, appears in the highest pressure region of ~ 270 GPa, present the strongest delocalization of O *s*-orbital and drastic change of O *p*-orbital, indicating pressure induced complex electronic structure near O atom.

Figure A2 present PDOS for excited state of the site resolved O atom in SiO_2 polymorphs. The spectrum feature are mostly comes from the O *p*-orbital in consist with the O *K*-edge XRS spectrum. This is because the excited 1s electron ascend to the *2p** state, and these energy, related to the O orbital, decide O *K*-edge XRS.

Appendix Ⅱ. C.V.

EDUCATION

2014. 8 ~ Candidates of M.S. Seoul National University, Korea. School of Earth and Environmental Sciences

2014. 8 B. S. Seoul National University, Korea. School of Earth and Environmental Sciences

RESEARCH EXPERIENCE

2014. 3 – 6 Teaching assistant

2015. 3 – 6 Teaching assistant

HONORS & AWARDS

2014. 7 전국지질연합필드 학술발표 최우수상

CONFERENCES

2014. 7 Atomistic origins of earthquake slip weakening (구두발표), 2014 년 전국지질연합필드

2014. 10 마찰용융에 기인한 규암 단층면 마찰계수 감소의 미시적 원인 (포스터), 2014 년 대한지질학회

2015. 5 양자화학계산을 이용한 SiO_2 고압상들의 전자구조 및 X-선 Raman 산란 스펙트럼 연구 (포스터), 2015 년 한국광물학회

2015. 10 기계적으로 비정질화된 규암의 미시적 구조 분석 (포스터), 2015 년 대한지질학회

국문 요약

지구상에서 가장 풍부한 물질인 실리카(SiO_2)는 지각과 맨틀을 구성하는 주요 성분으로 단층의 움직임에 영향을 미치거나 온도 압력 변화에 따른 구조 변화로 지구 내부 물성에 영향을 줄 수 있다. 이러한 실리카에 의한 지질학적 현상들은 실리카의 구조 변화에 기인한다. 실리카의 구조 변화는 온도 압력에 따른 변화뿐만 아니라 마찰과 같은 기계적인 에너지에 의해서도 크게 변하게 된다. 따라서 암석으로 이루어진 행성 내부의 물성이나 행성에서 일어나는 지질학적 현상들을 이해하기 위해선 여러 조건에 따라 변하는 실리카의 구조에 대한 미시적 이해가 필요하다.

본 연구에서는 실리카에 대한 두 가지 연구를 수행하였다. 첫 번째 연구는 실험적 방법론을 이용한 기계적 비정질화된 실리카에 대한 구조분석이다. 단층이 움직임에 따라 단층마찰면은 마찰력이 감소되는 현상이 나타나는데, 마찰면에서 형성되는 비정질 실리카와 이에 따른 실리카겔(silica gel)층의 형성이 그 현상의 원인 중 하나로 보고되고 있다. 비정질 실리카는 단층 마찰면에서 나타나는 마찰에 따른 에너지에 의해 작은 입자 형태로 형성되며, 이 과정 중에서 단층에 존재하던 물이나 주변 공기의 물과 반응을 하여 실리카 겔이 단층마찰면 표면에 형성 된다고 여겨진다. 석영질 암석을 이용한 마찰 실험을 통해 마찰에 따라 이러한 비정질 실리카와 실리카겔 형성 그리고 마찰계수의 감소가 보고 되었으며, 실제 자연 단층에서도 실리카겔 층에 대한 관찰이 보고 되었다. 하지만 복잡한 비정질 구조적 특성과 기존 분석 방법론적 한계로 비정질화된 실리카의 원자단위 구조와 기계적 비정질화 과정에 대한 미시적 기원이 정확히 규명되지 않았다. 이 연구에서는 실리카에 볼밀법으로 기계적 에너지를 가하면서 비정질화 시키고, 얻어진 비정질 구조를 특정 원자 주변의 구조에 대한 정량적인 분석이 가능한 고분해능 고상 핵자기 공명 분광 분석(nuclear magnetic resonance, NMR)을 이용하여 분석하였다. 또한

XRD, HR-TEM, EDS-mapping 방법 등을 이용하여, 비정질화 시킨 실리카의 형태와 다른 원소에 의해 생긴 상들이 존재하는지 분석하였다.

고상 핵 자기 공명 분광분석(NMR)은 특정 원자 주변의 짧은 단위의 원자환경까지 정밀하게 관찰할 수 있으며 원자단위의 결합에 대해 정량적인 정보를 제공하기 때문에 복잡한 비정질 구조에 대한 분석에 적합하다. 각기 다른 속도로 밀링한 비정질 실리카의 ^{29}Si MAS NMR 스펙트럼을 살펴보면, 600 rpm 이상으로 밀링한 샘플의 스펙트럼은 넓은 비정질 피크를 -80 ~ -120 ppm 에 걸쳐 뚜렷하게 보여준다. 특히 이 비정질 피크들은 기계적으로 비정질화된 실리카 내부 구조에 Q^2 와 Q^3 구조가 존재한다는 사실을 알려준다. 이렇게 얻어진 결과를 통해 실리카의 기계적 비정질화는 특정 에너지 이상에서만 나타난다는 사실을 추측할 수 있으며, 비정질화 과정에서 짧은 단위의 원자구조 변화와 함께 다른 물질과의 반응이 일어난다는 사실을 알 수 있다. 이렇게 얻어진 결과는 단층마찰면에서 용융을 수반하지 않고 나타나는 기계적 비정질화 과정과 생성된 비정질 실리카의 원자단위 구조에 대해 이해하는데 도움을 준다.

두 번째 연구는 컴퓨터 계산을 이용하여 결정질 실리카 동질이상들의 전자구조 분석과 스펙트럼 기원의 자세한 해석이다. 결정질 실리카는 온도 압력변화에 따라 다양한 결정 구조 변화를 거친다. 따라서 고온 고압환경의 암석질 행성 내부 구조를 이해하기 위해 고압상 실리카 구조에 대한 연구가 진행되어 왔다. *In situ* 고압상 전자구조 연구 중 가장 대표적인 방법이 diamond anvil cell 을 이용한 O *K*-edge x-ray Raman spectroscopy (XRS)인데, 실험적 한계로 ~70 GPa 이상에 대한 연구가 어려워 컴퓨터 계산 방법을 이용한 구조연구가 진행되고 있다. 하지만 O *K*-edge XRS 스펙트럼의 형태가 정확히 어떤 결정학적 요인에 의해 나타나는지 밝혀지지 않았다.

본 연구에서는 *ab initio* 계산을 통해 여러 결정질 동질이상 실리카에 대한 전자구조와 O *K*-dge XRS 스펙트럼을 계산하였으며, 스펙트럼의 형태 기원에 대한 분석을 하기 위해 결정학적 관계를 분석하였다. 이전 연구에 따르면 O *K*-edge XRS

스펙트럼 형태의 기원이 Si 원자의 배위수나 O 원자의 배위수에 기인한다고 주장되었다. 하지만 본 연구에서는 4 배위수 Si 을 가지는 hp-cristobalite 와 5 배위수 Si 을 가지는 penta-SiO_2 그리고 6 배위수 Si 을 가지는 stishovite 의 O *K*-edge XRS 스펙트럼의 형태가 유사하다는 사실을 밝혔으며, O 배위수가 각기 다른 penta-SiO_2 O *K*-edge XRS 스펙트럼 분석을 통해 원자의 배위수가 O *K*-edge XRS 스펙트럼 형태에 직접적인 영향을 끼치지 않는다는 사실을 알아냈다. 이렇게 얻어진 결과는 고압상 실리카의 전자구조에 대한 이해를 제공할 뿐만 아니라 O *K*-edge XRS 스펙트럼 해석에 대한 명확한 기준을 제시하여 준다.

Keywords: 실리카, 핵 자기 공명 분광분석(NMR), 볼밀, 기계적 비정질화, 고압상, 제 1 원리 계산, O *K*-edge XRS.